A meshfree adaptive procedure for shells in the sheet metal forming applications

Yong Guo [*1], C.T. Wu[1] and C.K. Park[2]

[1]*Livermore Software Technology Corporation, 7374 Las Positas Road, Livermore, CA 94551, USA*
[2]*National Crash Analysis Center (NCAC), The George Washington University, 45085 University Drive, Ashburn, VA 20147, USA*

Abstract.   In this paper, a meshfree shell adaptive procedure is developed for the applications in the sheet metal forming simulation. The meshfree shell formulation is based on the first-order shear deformable shell theory and utilizes the degenerated continuum and updated Lagrangian approach for the nonlinear analysis. For the sheet metal forming simulation, an h-type adaptivity based on the meshfree background cells is considered and a geometric error indicator is adopted. The enriched nodes in adaptivity are added to the centroids of the adaptive cells and their shape functions are computed using a first-order generalized meshfree (GMF) convex approximation. The GMF convex approximation provides a smooth and non-negative shape function that vanishes at the boundary, thus the enriched nodes have no influence outside the adapted cells and only the shape functions within the adaptive cells need to be re-computed. Based on this concept, a multi-level refinement procedure is developed which does not require the constraint equations to enforce the compatibility. With this approach the adaptive solution maintains the order of meshfree approximation with least computational cost. Two numerical examples are presented to demonstrate the performance of the proposed method in the adaptive shell analysis.

Keywords: meshfree; convex; shell; adaptivity; metal forming

1. Introduction

Recent developments in the meshfree methods add an additional dimension to computational mechanics (Belytschko *et al.* 1994, Liu *et al.* 1995a, Atluri and Zhu 1998, Chen *et al.* 1996, Wang and Chen 2004, Liu and Zhang 2008). Those methods do not rely on the traditional mesh-based approach to define the approximation functions. In comparison with the conventional finite element methods, the characteristics of smoothness and naturally conforming of the approximation, p-version of the intrinsic basis and higher convergence rate make the meshfree methods attractive alternative numerical techniques for industrial applications (Wang *et al.* 2009, Wu and Koishi 2009). Meshfree method using Moving Least-squares (MLS) (Lancaster and Salkauskas 1981, Belytschko *et al.* 1994) or Reproducing Kernel (RK) (Liu *et al.* 1995a, b) approximation has been successfully applied to the solid and structural analyses in the past decade (Chen and Wang 2006,

---

*Corresponding author, Ph.D., E-mail: yguo@lstc.com

Wang and Wu 2008, Wang and Lin 2011). However, the high computational cost of the meshfree approximations limits their applications to large-sized industrial problems, such as sheet metal forming simulations.

One way to solve large-sized industrial problems with desired accuracy and minimum cost is to adopt adaptive procedures in the simulation. In the nonlinear analysis of shell structures, the error introduced by the Galerkin method can be reduced to acceptable levels by means of suitable adaptation methods. Compared to the finite element method, the mesh-free method constructs the shape functions without the need of an explicit mesh. These shape functions are naturally conforming; therefore do not require the constraint equations to enforce the compatibility. Using the smooth approximation, the mesh-free method also provides a better fit to the real shell geometry. The error caused by the geometric approximation in the discretization of the curved shell is minimized and thus the meshfree approximation is ideal for adaptive computation.

Error indicators are used to control the adaptive procedure. There are two major errors in the discretization of a shell structure. The first error is caused by the finite functional approximations to the infinite dimensional functional space. This source of error is presented in any Galerkin method including the 2D and 3D finite element method and mesh-free method. The second error is related to the geometric approximation. Several error estimators have been developed and proved to be economical and effective in the work of solid finite element and mesh-free analysis (Deb 1996, Chung and Belytschko 1998). Some attempts of adaptivity for the finite element analysis of shells have also been developed (Baumann and Schweizerhof 1997, Riccius *et al.* 1997). Most of the works have been done using the recovery-based error estimators (Zienkiewicz and Zhu 1987) for the adaptive procedure. Nevertheless, they lack a sound theoretical background and are difficult to justify in the adaptive shell analysis. This is because the error estimators based on the projection or averaging procedures in the curved geometry have less physical meaning and may not be effective. The Babuska-Rheinboldt (BR) (Babuska and Rheinboldt 1978) and Zienkiewicz-Zhu (ZZ) (Zienkiewicz and Zhu 1987) criterions in the conventional error estimation are no longer appropriate due to the fact that the elements or projection planes are in general not on the same plane. A direct sampling procedure (Ortiz and Quigley 1991) does not require nodal projection and therefore does not ensure continuity of the internal variables. However, for bilinear quadrilaterals, the solution by the direct sampling procedure suffers serious noise and becomes corrupted. In addition, the error in the geometric approximation of a smoothed shell also needs to be minimized in the adaptive procedure. In the finite element method, the use of paving technique (Blacker and Stephenson 1991), local surface fitting, or any analytical description of the shell geometry can improve the geometric approximation in curved shells with considerable costs. Therefore, neither the residual type estimator nor the projection type estimator is rigorous and reliable. In this work, an error indicator based on the geometric change of the shell structure, for example, angle change (Hallquist 2003), will be adopted in the adaptive mesh-free shell method for its simplicity and robustness.

Three types of adaptivity are well developed, namely p-adaptivity, r-adaptivity and h-adaptivity. In p-adaptivity, higher order approximation functions or special enrichment functions are added in the numerical scheme. This type of adaptivity is widely used for simulating crack propagation problems (Moes *et al.* 1999, Pannachet *et al.* 2008). In r-adaptivity, the whole problem domain or a local region is remeshed and the new mesh is initialized from the old mesh using a least squares approximation (Liu and Tu 2002). In h-adaptivity, an element in the old mesh is divided into 4 elements in the refinement. The h-adaptivity is more suitable in 2D and shell problems because it is easy to maintain the mesh quality even with multiple levels of refinements. The advantage of

h-adaptivity in meshfree approximations also lies in the ease of implementation and the simplicity of the data structures (Rabczuk and Belystchko 2005). However, high computational cost is usually involved in the meshfree adaptivity. After the insertion of new nodes into the adaptive discretization, the shape functions at the added nodes and integration points, as well as at the affected original nodes and integration points have to be reconstructed. This requires extra loops for the neighboring searching. In addition, the global transformation matrix and its inverse have to be recomputed at each adaptive refinement. To reduce the high computational cost in the reconstruction of mesh-free shape functions as well as to pass the integration constraint (Wu and Guo 2002), Wu and Guo (2004) proposed a local enrichment on the adaptive mesh-free shape functions where the added points are finite element nodes that are enriched inside the adapted background cell. However, the solution accuracy is found to deteriorate when multiple levels of adaptivity are adopted, especially when the initial meshfree node distribution is coarse.

Recently several convex approximations were introduced (Sukumar 2004, Arroyo and Ortiz 2006) to improve the essential boundary condition treatment in the meshfree methods. The meshfree convex approximation guarantees the unique solution inside a convex hull with a minimum distributed data set and poses a weak Kronecker-delta property at the boundaries and therefore avoids the special treatments on the essential boundaries. Wu *et al.* (2011) provide a unified approach that is able to generate specific convex approximations as well as to reproduce several existing meshfree approximations, which is referred to as the generalized meshfree (GMF) approximation. In addition, they also found out that meshfree convex approximation behaves more robust than the conventional MLS approximation in terms of nodal support size, order of quadrature rule and discretization effects. It was shown that one can use larger time step for the meshfree convex approximation in the explicit dynamic analysis (Park *et al.* 2011). More recently, the meshfree convex approximation was introduced to the finite element method for solving the near-incompressible problems (Wu and Hu 2011, Wu *et al.* 2012) where an enriched point is added inside the finite element and its shape function is constructed by the meshfree convex approximation with the finite element nodes on its boundary. The resulting shape function of the enriched node has no influence outside its enriched element.

The objective of this work is to introduce a new meshfree adaptive procedure for shear deformable shells in industrial sheet metal forming applications. This paper is organized as follows: Section 2 reviews the basic theories. First the shear deformable shell model is given. Then the meshfree RKPM approximation is described and used to obtain the discrete equations for the shell model. The last part of this Section is to describe the generalized meshfree (GMF) convex approximation. In Section 3, the new meshfree h-adaptive procedure is presented. The GMF convex approximation is used to compute the shape functions at the added independent nodes. In Section 4, two numerical examples are presented. Final remarks are drawn in Section 5.

2. Basic theories

2.1 Shear deformable shell model

Consider a domain Ω of a shell which is consisted of the mid-plane reference surface $\overline{\Omega} \subset \Re^2$ with boundary Γ and a thickness t occupying the region $\overline{\Omega} \times \left(-t/2, t/2 \right)$ as shown in Fig. 1. The geometry and the kinematical fields of the shell can be described with the reference

surface and the fiber direction. The modified Mindlin-Reissner assumption requires that the motion and displacement of the shell are linear in the fiber direction (Belytcshko *et al.* 2000). The global coordinates and displacements at an arbitrary point within the shell body are given by

$$\boldsymbol{x} = \bar{\boldsymbol{x}} + \zeta \frac{h}{2} \boldsymbol{V}_3 \tag{1}$$

$$\boldsymbol{u} = \bar{\boldsymbol{u}} + \zeta \frac{h}{2} \boldsymbol{U} \tag{2}$$

where $\bar{\boldsymbol{x}}$ and $\bar{\boldsymbol{u}}$ are the position vector and translation displacement of the reference surface, respectively. $\boldsymbol{V}_3$ is the fiber director and $\boldsymbol{U}$ is the displacement resulting from the fiber rotation (see Figs. 1-2). h is the length of the fiber.

The mid-plane reference surface can be projected to a two-dimensional parametric plane. For an arbitrary shell surface defined by a finite element mesh, a parameterization algorithm, for example, the angle-based triangular flattening algorithm (Sheffer and de Sturler 2001), can be used to obtain the parametric representation of the shell surface.

With the parametric representation of the shell surface, a local co-rotational coordinate system ($\hat{x}$, $\hat{y}$, $\hat{z}$) can be defined on the shell reference surface, with $\hat{x}$ and $\hat{y}$ tangent to the reference surface and $\hat{z}$ in the thickness direction (see Fig. 1). The base vectors are given as

$$\hat{\boldsymbol{e}}_x = \frac{\boldsymbol{x}_{,\xi}}{\left\| \boldsymbol{x}_{,\xi} \right\|}, \qquad \hat{\boldsymbol{e}}_z = \frac{\boldsymbol{x}_{,\xi} \times \boldsymbol{x}_{,\eta}}{\left\| \boldsymbol{x}_{,\xi} \times \boldsymbol{x}_{,\eta} \right\|}, \qquad \hat{\boldsymbol{e}}_y = \hat{\boldsymbol{e}}_z \times \hat{\boldsymbol{e}}_x \tag{3}$$
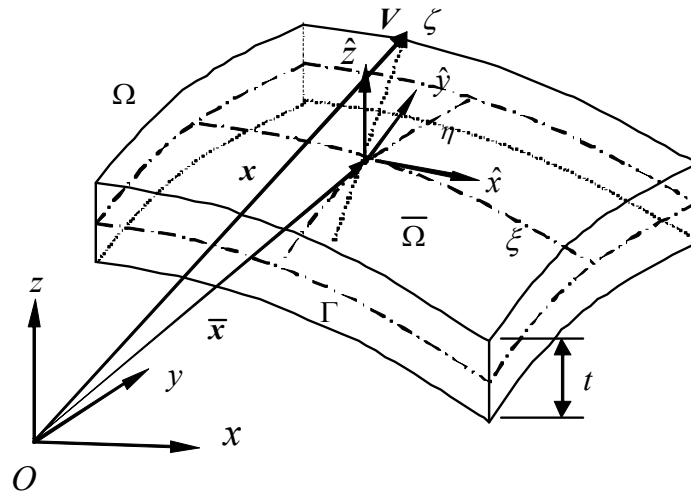
Fig. 1 Geometry of a shell
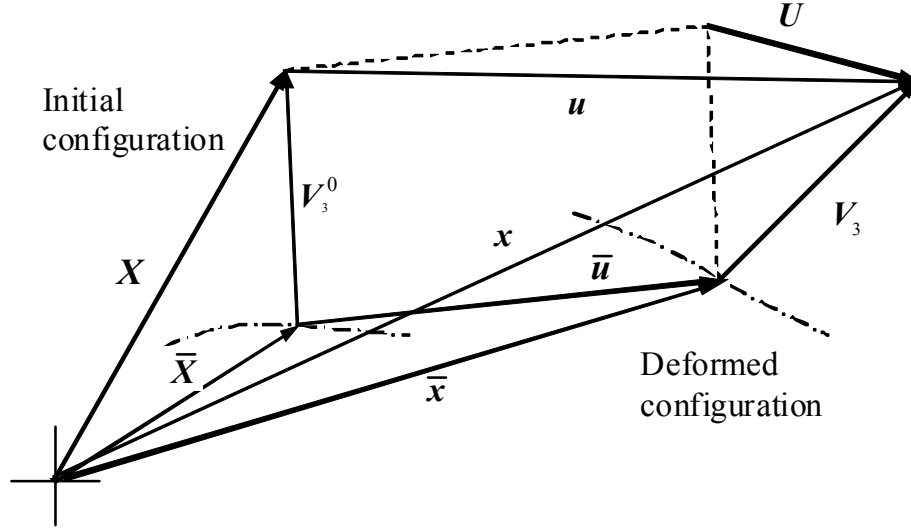
Fig. 2 Deformation of a shell

Let $\hat{\theta}_x$ and $\hat{\theta}_y$ be the rotations of the fiber director in the local co-rotational coordinate system, the displacement from the fiber rotation is expressed as

$$U = \begin{bmatrix} -\hat{e}_y & \hat{e}_x \end{bmatrix} \begin{Bmatrix} \hat{\theta}_x \\ \hat{\theta}_y \end{Bmatrix} \qquad (4)$$

The local rotations of the fiber director can be obtained from the global rotations by

$$\begin{Bmatrix} \hat{\theta}_x \\ \hat{\theta}_y \end{Bmatrix} = \begin{bmatrix} \hat{e}_x^T \\ \hat{e}_y^T \end{bmatrix} \begin{Bmatrix} \theta_x \\ \theta_y \\ \theta_z \end{Bmatrix} \qquad (5)$$

Further let $\hat{u}_0$, $\hat{v}_0$ and $\hat{w}_0$ denote the translation displacements of the mid-plane shell in the local $\hat{x}$, $\hat{y}$ and $\hat{z}$ directions, the displacement field $\hat{u} = \begin{bmatrix} \hat{u}, & \hat{v}, & \hat{w} \end{bmatrix}^T$ in the local co-rotational system at a at a typical point (ξ, η, ζ) may be represented as

$$\hat{u}(\xi,\eta,\zeta) = \begin{Bmatrix} \hat{u} \\ \hat{v} \\ \hat{w} \end{Bmatrix} = \begin{Bmatrix} \hat{u}_0(\xi,\eta) \\ \hat{v}_0(\xi,\eta) \\ \hat{w}_0(\xi,\eta) \end{Bmatrix} + \frac{\zeta h}{2} \begin{Bmatrix} \hat{\theta}_y(\xi,\eta) \\ -\hat{\theta}_x(\xi,\eta) \\ 0 \end{Bmatrix} = \begin{Bmatrix} \hat{u}_0(\xi,\eta) \\ \hat{v}_0(\xi,\eta) \\ \hat{w}_0(\xi,\eta) \end{Bmatrix} + \hat{z} \begin{Bmatrix} \hat{\theta}_y(\xi,\eta) \\ -\hat{\theta}_x(\xi,\eta) \\ 0 \end{Bmatrix} \qquad (6)$$

The strain components in the local co-rotational system can be decomposed into three parts by

$$\hat{\varepsilon} = \begin{Bmatrix} \hat{\varepsilon}_{xx} \\ \hat{\varepsilon}_{yy} \\ \hat{\gamma}_{xy} \\ \hat{\gamma}_{xz} \\ \hat{\gamma}_{yz} \end{Bmatrix} = \underbrace{\begin{Bmatrix} \dfrac{\partial \hat{u}_0}{\partial \hat{x}} \\ \dfrac{\partial \hat{v}_0}{\partial \hat{y}} \\ \dfrac{\partial \hat{u}_0}{\partial \hat{y}} + \dfrac{\partial \hat{v}_0}{\partial \hat{x}} \\ 0 \\ 0 \end{Bmatrix}}_{\hat{\varepsilon}_m} + \frac{\varsigma h}{2} \underbrace{\begin{Bmatrix} \dfrac{\partial \hat{\theta}_y}{\partial \hat{x}} \\ -\dfrac{\partial \hat{\theta}_x}{\partial \hat{y}} \\ \dfrac{\partial \hat{\theta}_y}{\partial \hat{y}} - \dfrac{\partial \hat{\theta}_x}{\partial \hat{x}} \\ 0 \\ 0 \end{Bmatrix}}_{\hat{\varepsilon}_b} + \underbrace{\begin{Bmatrix} 0 \\ 0 \\ 0 \\ \dfrac{\partial \hat{w}_0}{\partial \hat{x}} + \hat{\theta}_y \\ \dfrac{\partial \hat{w}_0}{\partial \hat{y}} - \hat{\theta}_x \end{Bmatrix}}_{\hat{\varepsilon}_s} \tag{7}$$

where $\hat{\varepsilon}_m$, $\hat{\varepsilon}_b$ and $\hat{\varepsilon}_s$ denote the membrane strain, bending strain and shear strain, respectively. The potential energy of a shell that undergoes deformations due to membrane, bending and shear can be written as

$$\Pi = \frac{1}{2}\int_{\Omega} \hat{\varepsilon}_m^T \boldsymbol{D}^m \hat{\varepsilon}_m d\Omega + \frac{1}{2}\int_{\Omega} \hat{\varepsilon}_b^T \boldsymbol{D}^b \hat{\varepsilon}_b d\Omega + \frac{1}{2}\int_{\Omega} \hat{\varepsilon}_s^T \boldsymbol{D}^s \hat{\varepsilon}_s d\Omega - \int_{\Omega} \rho \hat{\boldsymbol{u}}^T \ddot{\hat{\boldsymbol{u}}} d\Omega - W^{\text{ext}} \tag{8}$$

where $\boldsymbol{D}^m$ is the membrane rigidity, $\boldsymbol{D}^b$ is the bending rigidity and $\boldsymbol{D}^s$ is the shear rigidity. ρ is the density of the material and W^{ext} is the energy from the external forces.

The variational equation of a shear deformable shell can be expressed as

$$\int_{\Omega} \delta\hat{\varepsilon}_m^T \boldsymbol{D}^m \hat{\varepsilon}_m d\Omega + \int_{\Omega} \delta\hat{\varepsilon}_b^T \boldsymbol{D}^b \hat{\varepsilon}_b d\Omega + \int_{\Omega} \delta\hat{\varepsilon}_s^T \boldsymbol{D}^s \hat{\varepsilon}_s d\Omega - \int_{\Omega} \delta\hat{\boldsymbol{u}}^T \rho \ddot{\hat{\boldsymbol{u}}} d\Omega - \delta W^{\text{ext}} = 0 \tag{9}$$

2.2 Coupled FEM/ RKPM approximation

In the two dimensional case, a smooth function $\boldsymbol{u}$ at a point $\boldsymbol{x}$ is approximated using the following coupled FEM/RKPM method (Wang *et al.* 2009) given by

$$u_i(\boldsymbol{x}) \approx u_i^h(\boldsymbol{x}) = \sum_{\substack{I=1 \\ \boldsymbol{x}_I \in \Omega}}^{IP} \overline{w}_a^{[n]}(\boldsymbol{x}; \boldsymbol{x} - \boldsymbol{x}_I) d_{iI} + \sum_{\substack{L=1 \\ \mathrm{x}_L \in \Gamma}}^{MP} N_L^{[m]}(\boldsymbol{x}) d_{iL}; \forall \ \boldsymbol{x} \in \Omega \subset \mathfrak{R}^2 \tag{10}$$

where Ω denotes a mesh-free domain bounded in $\mathfrak{R}^2$. Γ is an interface between meshfree domain and finite element domain or an essential boundary, where we set the nodes on the interface or boundary as finite element nodes (Wang *et al.* 2009). $\overline{w}_a^{[n]}$ is called the reproducing kernel function (Liu *et al.* 1995a) where n denotes the order of the basis functions and 'a' is the support size of the kernel. $N_L^{[m]}$ is the standard finite element shape function with interpolation order m. *IP* is the number of mesh-free particles that influence the solution at point $\boldsymbol{x}$. d_{iI} is the coefficient of the approximation and in general, is not equal to the value of the function at the node. *MP* is the number of interface or boundary nodes that influence the approximation. The reproducing kernel function has to satisfy the *n*th-order reproducing conditions

$$\sum_{\substack{I=1 \\ x_I \in \Omega}}^{IP} \overline{w}_a^{[n]}(\boldsymbol{x}; \boldsymbol{x} - \boldsymbol{x}_I) x_{1I}^{\alpha} x_{2I}^{\beta} + \sum_{\substack{J=1 \\ x_J \in \Gamma}}^{MP} N_J^{[m]}(\boldsymbol{x}) x_{1J}^{\alpha} x_{2J}^{\beta} = x_1^{\alpha} x_2^{\beta}, \ \alpha + \beta = 0,\dots,n \tag{11}$$

Therefore, the solution approximation can be expressed in the following form

$$u_i^{\,h}(\boldsymbol{x}) = \sum_{\substack{I=1 \\ x_I \in \Omega}}^{IP} \overline{\Psi}_I(\boldsymbol{x}) d_{iI} + \sum_{\substack{J=1 \\ x_J \in \Gamma}}^{MP} N_J^{[m]}(\boldsymbol{x}) d_{iJ} = \sum_{I=1}^{NP} \widetilde{\Psi}_I(\boldsymbol{x}) d_{iI}; \forall\, \boldsymbol{x} \in \Omega \cup \Gamma \tag{12}$$

with *NP* being the total number of mesh-free and interface nodes that influence the solution at point *x* and

$$\overline{\Psi}_I(\boldsymbol{x}) = \Psi_I(\boldsymbol{x}) - \sum_{\substack{J=1 \\ x_J \in \Gamma}}^{MP} \boldsymbol{H}^{[n]^T}(\boldsymbol{x} - \boldsymbol{x}_J) \boldsymbol{M}^{[n]^{-1}}(\boldsymbol{x}) \boldsymbol{H}^{[n]}(\boldsymbol{x} - \boldsymbol{x}_I) w_a(\boldsymbol{x} - \boldsymbol{x}_I) N_J^{[m]}(\boldsymbol{x}) \tag{13}$$

where $\Psi_I(\boldsymbol{x})$ is the conventional mesh-free shape function, $\boldsymbol{M}^{[n]}(\boldsymbol{x})$ is the moment matrix and $\boldsymbol{H}^{[n]}(\boldsymbol{x} - \boldsymbol{x}_I)$ is a vector of polynomials up to order *n*.

When the finite element interpolation order *m* is equal to the reproducing order *n*, we have

$$\overline{\Psi}_I(\boldsymbol{x}) = 0 \ \text{ for all nodes } \ \{I : supp(\Psi_I) \cap \Gamma \neq 0\} \text{ and } \ \boldsymbol{x} \in \Gamma \tag{14}$$

The shape functions on the interface or essential boundary are reduced to the standard finite element shape functions and possess the Kronecker-delta property.

2.3 Discrete equations of meshfree shell

With the meshfree approximation described in the previous Section, the motion of the mid-plane surface and the displacements of the shell in the local co-rotational coordinate system are approximated by

$$\hat{x}_i = \sum_{I=1}^{NP} \widetilde{\Psi}_I(\xi,\eta) \hat{x}_{iI} \tag{15}$$

$$\hat{\boldsymbol{u}} = \sum_{I=1}^{NP} \widetilde{\Psi}_I(\xi,\eta) \begin{Bmatrix} \hat{u}_{0I} \\ \hat{v}_{0I} \\ \hat{w}_{0I} \end{Bmatrix} + \zeta \sum_{I=1}^{NP} \widetilde{\Psi}_I(\xi,\eta) \frac{h_I}{2} \begin{Bmatrix} \hat{\theta}_{yI} \\ -\hat{\theta}_{xI} \\ 0 \end{Bmatrix} \tag{16}$$

The meshfree shape functions are constructed in the parametric plane. To satisfy the linear exactness in the approximation, the Lagrangian smoothed strains (Chen *et al.* 2001) are used and given by

$$\widetilde{\boldsymbol{\varepsilon}}^{m} = \sum_{I} \widetilde{\boldsymbol{B}}_{I}^{m} \hat{\boldsymbol{d}}_{I}, \quad \widetilde{\boldsymbol{\varepsilon}}^{b} = \zeta \sum_{I} \widetilde{\boldsymbol{B}}_{I}^{b} \hat{\boldsymbol{d}}_{I}, \quad \widetilde{\boldsymbol{\varepsilon}}^{s} = \sum_{I} \widetilde{\boldsymbol{B}}_{I}^{s} \hat{\boldsymbol{d}}_{I} \tag{17}$$

where the smoothed strain operators are calculated by averaging the consistent strain operators over an area A around the evaluated point

$$\widetilde{\boldsymbol{B}}_{I}^{m}(\boldsymbol{x}_{I}) = \frac{1}{A_{I}} \int_{\Omega_{I}} \hat{\boldsymbol{B}}_{I}^{m} dA, \quad \widetilde{\boldsymbol{B}}_{I}^{b}(\boldsymbol{x}_{I}) = \frac{1}{A_{I}} \int_{\Omega_{I}} \hat{\boldsymbol{B}}_{I}^{b} dA, \quad \widetilde{\boldsymbol{B}}_{I}^{s}(\boldsymbol{x}_{L}) = \frac{1}{A_{L}} \int_{\Omega_{L}} \hat{\boldsymbol{B}}_{I}^{s} dA \tag{18}$$

and $\hat{\boldsymbol{d}}_{I}$ is a vector consisting of the five local degrees-of-freedom

$$\hat{\mathbf{d}}_{I} = \begin{bmatrix} \hat{u}_{0I} & \hat{v}_{0I} & \hat{w}_{0I} & \hat{\theta}_{xI} & \hat{\theta}_{yI} \end{bmatrix}^{T} \tag{19}$$

The local consistent membrane, bending and shear strain operators $\hat{\boldsymbol{B}}_{I}^{m}$, $\hat{\boldsymbol{B}}_{I}^{b}$ and $\hat{\boldsymbol{B}}_{I}^{s}$ can be computed from Eq. (7).

Substituting Eqs. (16) and (17) into the variational equation Eq. (9) and transforming the results from the local co-rotational coordinate system to the global system, we have the discrete equations of the shear deformable meshfree shell in the global coordinate system

$$\boldsymbol{M}\ddot{\boldsymbol{d}} = \boldsymbol{F}^{\text{int}} - \boldsymbol{F}^{ext} \tag{20}$$

where M is the consistent mass matrix, which needs to be lumped in the transient dynamic explicit analysis, $\boldsymbol{F}^{ext}$ is the nodal force resulting from the external loading and $\boldsymbol{F}^{\text{int}}$ is the internal nodal force which, in the local co-rotational coordinate system, is given by

$$\hat{\boldsymbol{F}}_{I}^{\text{int}} = \int_{\Omega} \widetilde{\boldsymbol{B}}_{I}^{m^{T}} \hat{\boldsymbol{\sigma}} d\Omega + \int_{\Omega} \zeta \widetilde{\boldsymbol{B}}_{I}^{b^{T}} \hat{\boldsymbol{\sigma}} d\Omega + \int_{\Omega} \widetilde{\boldsymbol{B}}_{I}^{s^{T}} \hat{\boldsymbol{\sigma}} d\Omega \tag{21}$$

In order to avoid shear locking in the analysis of thin shells, the shear nodal force (third term in Eq. (21)), should be under-integrated by using one integration point in each background cell (Wu and Guo 2002).

Since the meshfree shape functions do not possess Kronecker-delta property, the real displacements at the meshfree nodes have to be computed with the meshfree approximation, Eq. (12) as

$$\boldsymbol{u}^{h}(\boldsymbol{x}_{I}) = \boldsymbol{u}_{I}^{h} = \sum_{J=1}^{NP} \widetilde{\Psi}_{J}(\boldsymbol{x}_{I}) \boldsymbol{d}_{J} \tag{22}$$

or in matrix form as

$$\boldsymbol{d}^{h} = \boldsymbol{A}\boldsymbol{d} \tag{23}$$

where A is called the transformation matrix and is used to transform both the displacements and nodal forces between the real values and the meshfree nodal values.

2.4 Generalized meshfree (GMF) convex approximation

In this Section, a first-order generalized meshfree (GMF) convex approximation is introduced to the enriched nodes as will be described in Section 3.2 for the h-adaptive procedure. The fundamental idea of the GMF approximation (Wu *et al.* 2011) is the introduction of an enriched basis function in the Shepard function (Shepard 1968) to achieve the linear consistency. The choice of the basis function determines whether the GMF approximation has convexity property.

Assume a convex hull *conv* (Λ) of a node set $\Lambda = \{x_i, i = 1, \cdots n\} \subset \Re^2$ defined by (Wu *et al.* 2011)

$$Conv\,(\Lambda) = \left\{ \sum_{i=1}^{n} \alpha_i \boldsymbol{x}_i \, \middle| \, \boldsymbol{x}_i \in \Lambda, \ \alpha_i \in \Re \ , \alpha_i \geq 0, \ \sum_{i=1}^{n} \alpha_i = 1, i = 1,2, \cdots \right\} \tag{24}$$

The GMF method is to construct the approximation of a given function $\boldsymbol{u}$ in the form

$$\boldsymbol{u}^h(\boldsymbol{x}) = \sum_{i=1}^{n} \Phi_i(\boldsymbol{x}) \boldsymbol{u}_i \tag{25}$$

with the generating function $\Phi_i : \boldsymbol{conv}(\Lambda) \to \Re$ satisfying the following polynomial reproduction property

$$\sum_{i=1}^{n} \Phi_i(\boldsymbol{x}) \boldsymbol{x}_i = \boldsymbol{x} \ \forall \ \boldsymbol{x} \in \boldsymbol{conv}(\Lambda) \tag{26}$$

The first-order GMF approximation in multiple dimensions is expressed as
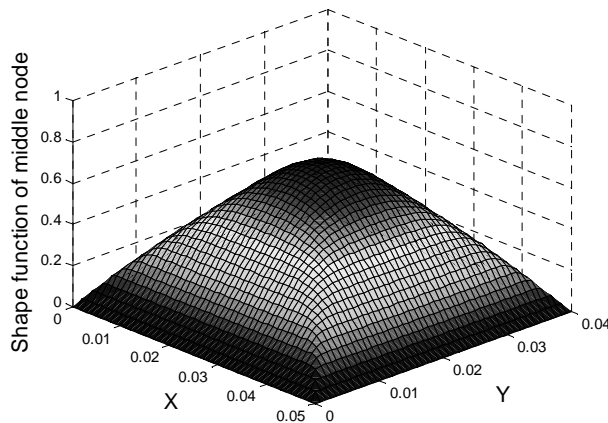
Fig. 3 First-order convex shape function at center node with four boundary nodes

$$\Phi(\boldsymbol{x}, \lambda_r) = \frac{\Psi_i}{\Psi} = \frac{\phi_a(\boldsymbol{x}; \boldsymbol{X}_i) \mathrm{B}_i(\boldsymbol{X}_i, \lambda_r)}{\sum_{j=1}^{n} \phi_a(\boldsymbol{x}; \boldsymbol{X}_j) \mathrm{B}_j(\boldsymbol{X}_j, \lambda_r)} \tag{27}$$

subjected to the following linearity constraints

$$\boldsymbol{R}_r(\boldsymbol{x}, \lambda_r) = \sum_{i=1}^{n} \Phi_i \boldsymbol{X}_i = 0 \tag{28}$$

where $\phi_a(\boldsymbol{x}, \boldsymbol{X}_i)$ is the weight function of node i with support size $supp(\phi_a(\boldsymbol{x}; \boldsymbol{X}_i)) = a_i$, $\mathrm{B}(\boldsymbol{X}_i, \lambda_r)$ is the basis function of the GMF approximation, $\boldsymbol{X}_i = \mathbf{x} - \mathbf{x}_i$ and

$$\Psi_i = \phi_a(\boldsymbol{x}; \boldsymbol{X}_i) \mathrm{B}_i(\boldsymbol{X}_i, \lambda_r) \tag{29}$$

$$\Psi = \sum_{j=1}^{n} \phi_a(\boldsymbol{x}; \boldsymbol{X}_j) \mathrm{B}_j(\boldsymbol{X}_j, \lambda_r) \tag{30}$$

n is the number of nodes within the support size $a(\boldsymbol{x})$ at fixed $\boldsymbol{x}$, $\lambda_r(\boldsymbol{x}) (r = 1, 2, \cdots, m)$ are constraint parameters which have to be decided and m is the number of constraints ($m = 1$ in 1D, $m = 2$ in 2D and $m = 3$ in 3D).

In the GMF approximation, the property of the partition of unity is automatically satisfied by the normalization in Eq. (27). The completion of the GMF approximation is achieved by finding λ_r to satisfy Eq. (28). To determine λ_r at any fixed x in Eq. (28), a root-finding algorithm is required for the non-linear basis functions. Usually, the Newton-Raphson method is considered for the equation solving of the objection function in Eq. (28).

(a) Center node *N*1   (b) Mid-edge node *N*2
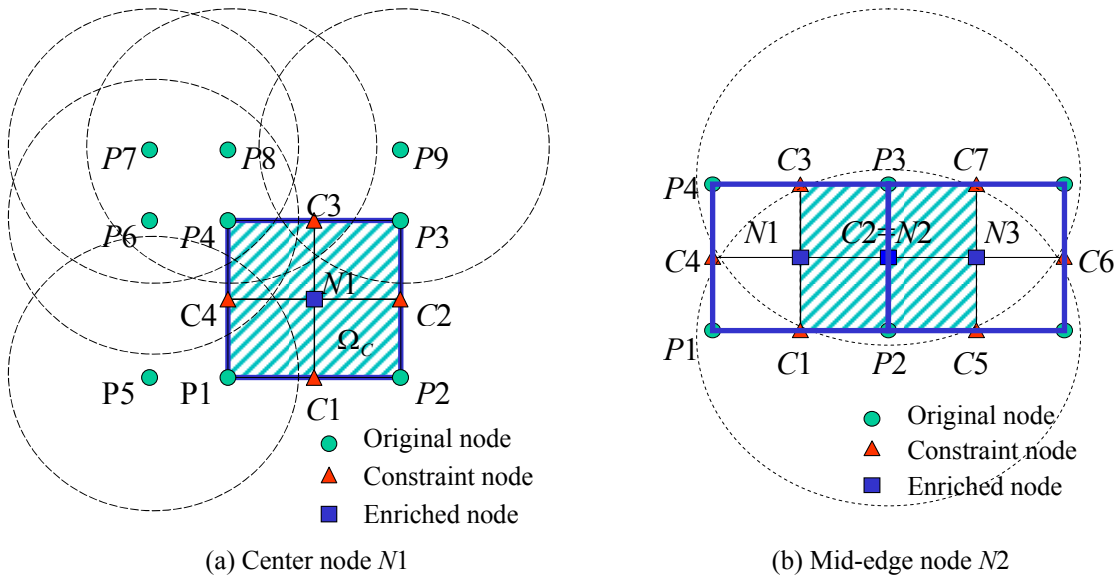
Fig. 4 First level adaptivity

The convexity of the GMF approximation is determined by the selection of a positive basis function in Eq. (27). Another property of the convex approximation is that the shape functions of the interior points will vanish at the boundary nodes. The proof of the weak Kronecker-delta property at the boundaries in convex approximation can be found in Wu *et al.* (2011). A typical first-order meshfree convex shape function at the center point is shown in Fig. 3. In this paper, a convex GMF approximation is constructed by using an inverse tangent basis function and a cubic spline function with a rectangular support is chosen to be the weight function in Eq. (27).

3. Meshfree adaptive procedure for shells

In this Section, we describe a meshfree adaptive procedure for the applications in the sheet metal forming simulation. The challenges in the adaptive refinement procedure include the satisfaction of compatibility in approximation (shape function) and satisfaction of integration constraint in spatial integration. Finite element method with linear approximation enforces both compatibility and integration constraint using the so-called "constraint of compatibility" (Belytschko and Tabbara 1993). For mesh-free method, although the compatibility is naturally enforced during the adaptive refinement, the integration constraint is difficult to impose.

Since the mesh-free shape functions are reconstructed, the constraints of compatibility after enrichment are not required. In this work, the proposed local enrichment in the adaptive refinement not only improves the computational cost, it also enforces the integration constraint during the mesh-free adaptive procedure.

3.1 Error indicators

In order to control the adaptive procedure the error indicators must be available. There are two major errors in the discretization of a shell structure. The first error is caused by the finite functional approximations to the infinite dimensional functional space and the standard error estimators are available. The second error is related to the geometric approximation. The Babuska-Rheinboldt (BR) (Babuska and Rheinboldt 1978) and Zienkiewicz-Zhu (ZZ) (Zienkiewicz and Zhu 1987) criterions in the conventional error estimation are no longer appropriate due to the fact that the elements or projection planes are in general not on the same plane. Thus neither the residual type estimator nor the projection type estimator is rigorous and reliable.

On the other hand, in the sheet metal forming process, the blank is compressed by the dies and undergoes geometric changes. More severe the geometry of the blank shell changes, finer mesh it requires to capture the large deformation. Therefore, the geometric change of the blank serves as an indicator when and where the mesh refinement should be.

In this work, an error indicator based on the geometric change such as the angle change (Hallquist 2003) is adopted in the adaptive mesh-free shell method for its simplicity and robustness.

3.2 Refinement procedure

In the meshfree shell formulation, the shell surface is mapped to a parametric reference plane.

The background cells are defined on the parametric plane and they serve as integration cells for the computation of the stiffness matrices and internal nodal forces. The meshfree adaptive process is conducted on the background cells.

In a meshfree refinement procedure, the background cell that is identified by the error indicator is divided into four sub-cells. New nodes are added at the center and at the mid-points of four sides as shown in Fig. 4(a). In a first level adaptivity, an original background cell *P*1-*P*2-*P*3-*P*4 is divided into four sub-cells by inserting one center node *N*1 and four mid-points *C*1, *C*2, *C*3 and *C*4. The center node *N*1 is an enriched point inside the background cell *P*1-*P*2-*P*3-*P*4. The four mid-points are called constraint points in this paper but they are different from the constraint points in the finite element adaptivity, which we will show later. The mid-point between two neighboring adapted background cells becomes an enriched point as shown in Fig. 4(b), where the mid-point *C*2 becomes *N*2 which is an enriched node in the adaptive cell formed by *C*1-*C*5-*C*7-*C*3. In Figs. 4 and 5, the circular green dots indicate the original meshfree nodes, blue squares are the enriched nodes and red triangles the constraint nodes.

Multiple level of refinement is shown in Fig. 5. In the second level adaptivity, sub-cell *A*1 is divided into four cells and the center node *N*6 is the enriched node in cell *A*1. In order to maintain mesh quality, the adaptive level of any neighboring cells should not be greater than 1. Background cells *B* and *C* have to be adapted (first level adaptivity) and constraint nodes *C*3 and *C*4 become new enriched nodes *N*3 and *N*2.

The shape function of the enriched nodes is computed using GMF convex approximation described in Section 2.4, with the enriched node at the center and the four corner nodes of the enriched background cell being the boundary nodes. For example, the shape function of node *N*1 is computed with nodes *P*1, *P*2, *P*3 and *P*4 as its boundary nodes. However, the convex shape function does not have the Kronecker-delta property but it can be normalized as in the following equation to possess the property

$$\widetilde{\Phi}_L(\xi) = \Phi_L(\xi) / \Phi_L(\xi_L) \tag{31}$$
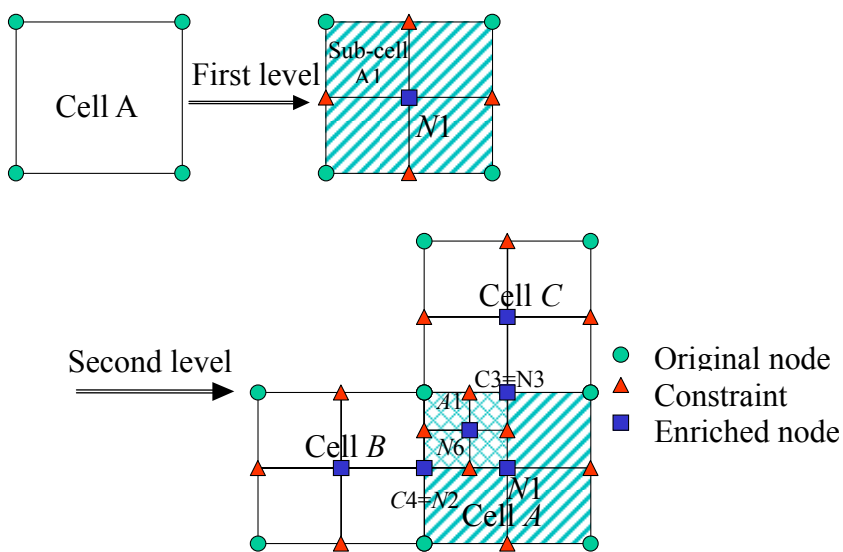
Fig. 5 Multiple level adaptivity

where $\Phi_L(\xi)$ is the shape function of the enriched node L computed from the GMF convex approximation, $\Phi_L(\xi_L)$ is the shape function at node ξ_L. ξ is the parametric coordinate. Since the normalized shape functions of the enriched nodes have the Kronecker-delta property, the real displacements at the enriched nodes and the nodal displacements are the same so the transformation matrix in Eq. (23) does not need to be re-computed. Also the influence domain of the enriched nodes is limited to the enriched background cells, the shape functions outside the enriched background cells do not need to be re-constructed. These properties will save tremendous computational time.

At the constraint nodes the mesh-free shape functions are chosen to be the average of the shape functions of the two nodes on the edge to satisfy the integration constraints (Wu and Guo 2002, Wang *et al.* 2009) in order to pass the constant stress patch test, as following

$$\psi_I(\xi_{CI}) = \frac{1}{2}\left(\widetilde{\Psi}_I(\xi_{P1}) + \widetilde{\Psi}_I(\xi_{P2})\right) \tag{32}$$

where *CI* is a constraint node and *P1* and *P2* are two edge points.

In each adaptive cell the meshfree shape functions need to be re-constructed. Similarly as in Section 2.2, the approximation of a function *u* is expressed as

$$u_i^h(\xi) = \sum_{\substack{I=1 \\ \xi_I \in \Omega}}^{IP} \overline{w}_a^{[n]}(\xi; \xi - \xi_I)d_{iI} + \sum_{\substack{L=1 \\ \xi_L \in \Omega}}^{EP} \widetilde{\Phi}_L^{[n]}(\xi)d_{iL} + \sum_{\substack{K=1 \\ \xi_K \in \Omega}}^{CP} \psi_K^{[n]}(\xi)d_{iK}; \forall\ \xi \in \Omega_C \subset \mathfrak{R}^2 \tag{33}$$

where $\Omega \subset \mathfrak{R}^2$ is the domain of the shell in the parametric reference plane, Ω_C is the adaptive cell, *EP* is the number of enriched points influencing on the evaluating point ξ and $\widetilde{\Phi}_L^{[n]}$ is the normalized enrichment shape function in Eq. (31), *CP* is the number of constraint nodes influencing on ξ and $\psi_K^{[n]}$ is the shape functions of the constraint nodes. The kernel function $\overline{w}_a^{[n]}$ has to satisfy the reproducing conditions

$$\sum_{\substack{I=1 \\ \xi_I \in \Omega}}^{IP} \overline{w}_a^{[n]}(\xi; \xi - \xi_I)\xi_I^\alpha \eta_I^\beta + \sum_{\substack{J=1 \\ \xi_J \in \Omega}}^{EP} \widetilde{\Phi}_J^{[n]}(\xi)\xi_J^\alpha \eta_J^\beta + \sum_{\substack{K=1 \\ \xi_K \in \Omega}}^{CP} \psi_K^{[n]}(\xi)\xi_K^\alpha \eta_K^\beta = \xi^\alpha \eta^\beta,\ \alpha + \beta = 0,\ldots,n \tag{34}$$

The approximation Eq. (33) is then derived to be

$$u_i^h(\xi) = \sum_{\substack{I=1 \\ \xi_I \in \Omega}}^{IP} \overline{\Psi}_I(\xi)d_{iI} + \sum_{\substack{J=1 \\ \xi_J \in \Omega}}^{EP} \widetilde{\Phi}_J^{[n]}(\xi)d_{iJ} + \sum_{\substack{K=1 \\ \xi_K \in \Omega}}^{CP} \psi_K^{[n]}(\xi)d_{iK} = \sum_{I=1}^{NP} \widetilde{\Psi}_I(\xi)d_{iI}; \forall \xi \in \Omega_C \tag{35}$$

where the shape functions of the original meshfree nodes are

$$\overline{\Psi}_I(\xi) = \Psi_I(\xi) - \sum_{\substack{J=1 \\ \xi_J \in \Omega}}^{EP} \boldsymbol{H}^{[n]^T}(\xi - \xi_J)\boldsymbol{M}^{[n]^{-1}}(\xi)\boldsymbol{H}^{[n]}(\xi - \xi_I)w_a(\xi - \xi_I)\widetilde{\Phi}_J^{[n]}(\xi)$$
$$- \sum_{\substack{K=1 \\ \xi_K \in \Omega}}^{CP} \boldsymbol{H}^{[n]^T}(\xi - \xi_J)\boldsymbol{M}^{[n]^{-1}}(\xi)\boldsymbol{H}^{[n]}(\xi - \xi_I)w_a(\xi - \xi_I)\psi_K^{[n]}(\xi) \tag{36}$$

The locations of the new nodes in the real geometry can be computed by using the mesh-free approximation

$$x = \sum_{I=1}^{NP} \widetilde{\Psi}_I(\xi) x_I \tag{37}$$

Correspondingly a four-noded background element in the shell surface is adapted into four sub-elements. Unlike the finite element adaptivity, the sub-planes defined by the four sub-elements are not necessarily on the same plane of the original element in the real geometry due to the fact that the geometric approximation is no more linear in the mesh-free shell formulation. Therefore, the geometry can be better described by the adaptive mesh-free shells. This is one of the major differences between the adaptive mesh-free and finite element shells.

3.3 Transfer of variables

During the process of transfer, the stresses and internal variables at the stress points of the original discretization are subjected to a 'smoothing' operation before being transferred to the new adaptive discreatization. In finite element method, the smoothed continuous stress field is derived from the discontinuous finite element stress. Usually a "stress projection method" (Zienkiewicz and Zhu 1987) is adopted and an averaged C_0-nodal stress (Mar and Hicks 1996) is required.

Typically a nodal projection is used in the smoothing operation. Similar to the finite element method, a simple weighted averaging procedure within the co-rotational configuration is used for the nodal projection. After the stresses and internal variables have been transferred to the nodes,
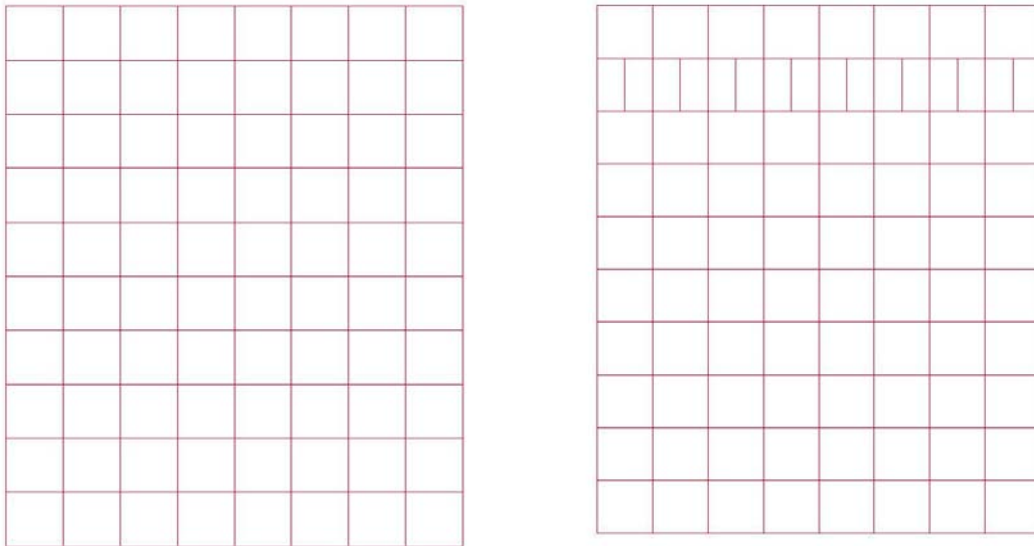
| (a) Regular mesh | (b) Regular mesh with constraints |

Fig. 6 Two meshes used in plate necking problem

they will be recovered at the new stress points on the adaptive discretization using the newly constructed mesh-free interpolation and the continuity will be ensured.

The transfer of variables involves the attainment of smoothed variable fields by projection onto the mesh-free shape function $\tilde{\Psi}$. For example, the new stresses can be obtained using the expression

$$\sigma^* = \tilde{\Psi}\bar{\sigma}^* \tag{38}$$

where $\bar{\sigma}^*$ are the smoothed nodal stresses using a weighted averaging given by

$$\bar{\sigma}^{*j} = \sum_{I=1}^{IE} w_I \sigma_I^{\ j} \tag{39}$$

$\bar{\sigma}^{*j}$ is the j-th component of the smoothed nodal stresses, $\sigma_I^{\ j}$ is the j-th component of the local stress evaluated at the stress point of co-rotation plane I and w_I is the weight.

4. Numerical examples

4.1 Plate stretching

The first example is a benchmark of a plate under stretching. This benchmark is selected to ensure that the mesh-free local enrichment can represent the continuous stress state without deterring the physics due to the adaptive procedure. An aluminum plate is fixed on the bottom and subjected a prescribed displacement on the top. Only half of the specimen is modeled and two mesh densities are used in this problem as shown in Fig. 6: a regular mesh and an adaptive mesh with constrained nodes. In these models the bottom nodes are constrained and the top nodes are subjected to pulling displacements.

Fig. 7 shows the predicted load responses by the finite element and meshfree methods. As shown in Fig. 7(a), the necking behavior is suppressed in the adaptive model due to the constraint
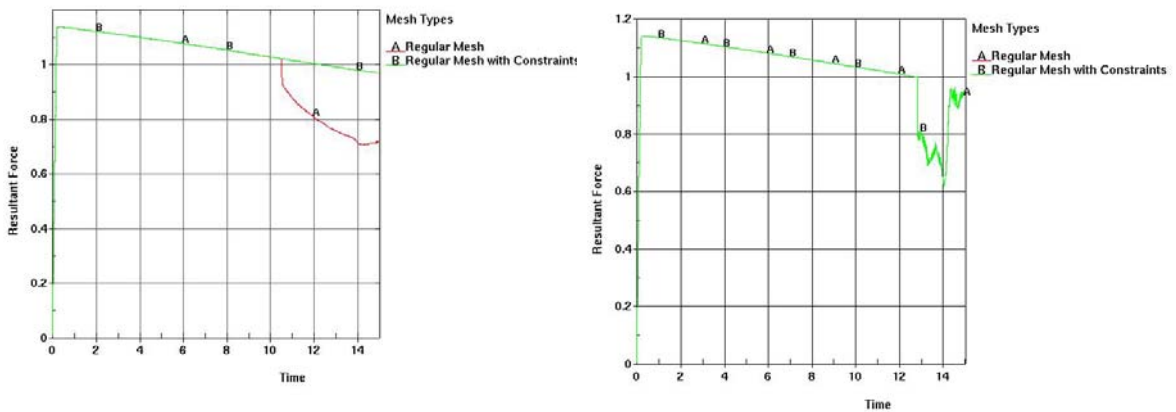
(a) Load responses by finite element   (b) Load responses by mesh-free

Fig. 7 Load responses of the necking plate
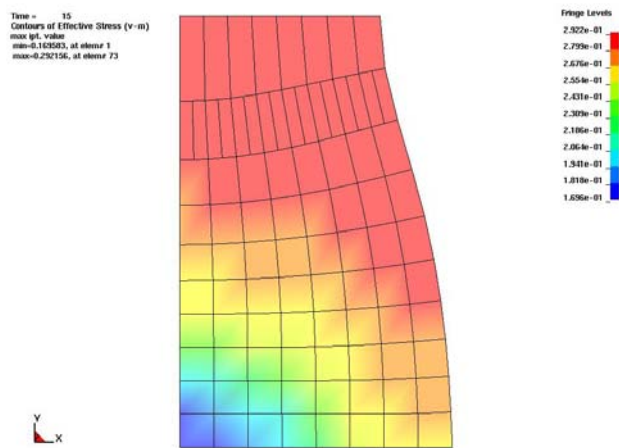
Fig. 8 Final shape and stress contour of the necking plate
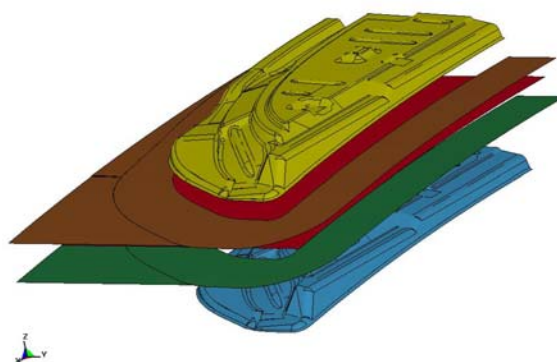
Fig. 9 Model setup for door panel forming
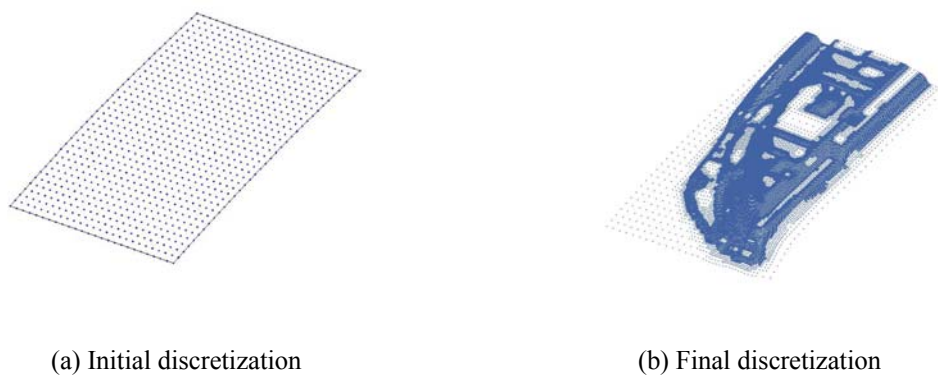
(a) Initial discretization   (b) Final discretization
Fig. 10 Initial and final discretizations of the work piece

(a) Meshfree adaptivity   (b) Finite element adaptivity
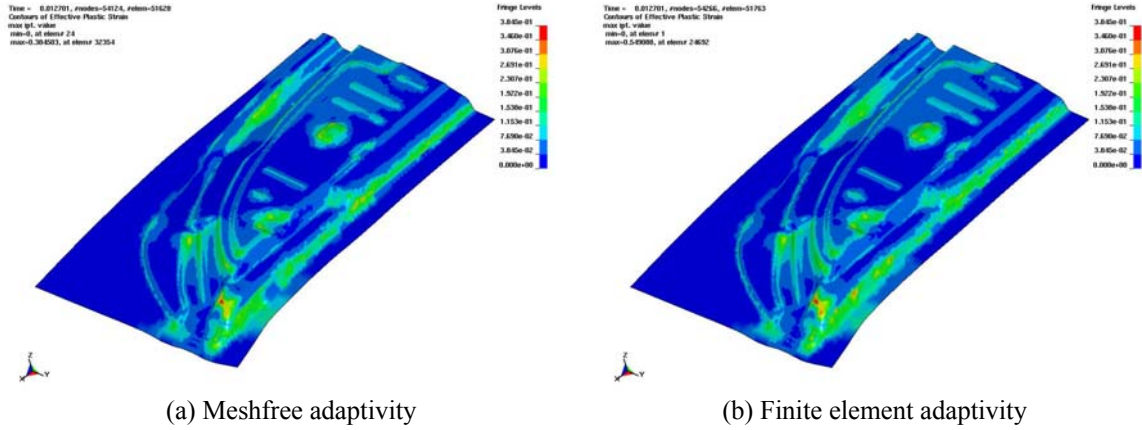
Fig. 11 Comparison of effective plastic strain in final shape

effect imposed by the finite element compatibility. On the other hand, the load response from the mesh-free adaptive model is compared well with the regular mesh. This is because no "constraint of compatibility" is required in the mesh-free adaptive procedure and the necking phenomena can be properly captured. The final deformation and stress contour are also displayed in Fig. 8 for the present method.

4.2 Door panel forming

Forming of an automobile door panel is simulated in this example. The model setup is shown in Fig. 9. The work piece, a blank (the red part in Fig. 9) with a length of 860 mm, a width of 605 mm and a thickness of 0.66 mm, is held by the upper and lower binders (the brown and green parts) over the die (the blue part) and deformed by the punch (the yellow part) when the punch moves down. The work piece is made of mild steel and is modeled by a transversely anisotropic elastic-plastic constitutive law (Hill 1948) with the following material constants: density $\rho = 7.8 \times 10^{-9}$ ton/mm^3, Young's modulus $E = 2.07 \times 10^5$ N/mm^2, Poisson's ratio $\gamma = 0.28$, yield stress $\sigma_y = 166$ N/mm^2, plastic hardening modulus $E_p = 524$ N/mm^2 and anisotropic hardening parameter (the ratio of the in-plane plastic strain rate to the out-of-plane plastic strain rate) R=1.65. The binders, the die and the punch are modeled as non-deformable rigids.

Both the meshfree adaptivity presented in this paper and the finite element adaptivity are used to simulate the forming process. Cubic spline kernel function with rectangular support domain and normalized support size of 1.2 in both $\xi-$ and $\eta-$directions is used for the construction of the meshfree shape functions. In the meshfree model, the work piece is discretized with 962 uniformly distributed meshfree nodes (see Fig. 10(a)) while it is discretized with 900 regular elements in the finite element model. The maximum level of adaptivity is 4 and in the final formed panel, the number of nodes is increased to 34,084 for the meshfree adaptivity as shown in Fig. 10(b) while the number of elements is increased to 32,943 for the finite element adaptivity. The CPU time of the meshfree adaptivity is 54% more than the finite element adaptivity, which is acceptable by the industrial standard.

A comparison of the effective plastic strain in the final formed shape is given in Fig. 11. The maximum effective plastic strain obtained from the meshfree adaptivity is 0.38 and from the finite

(a) Meshfree adaptivity   (b) Finite element adaptivity
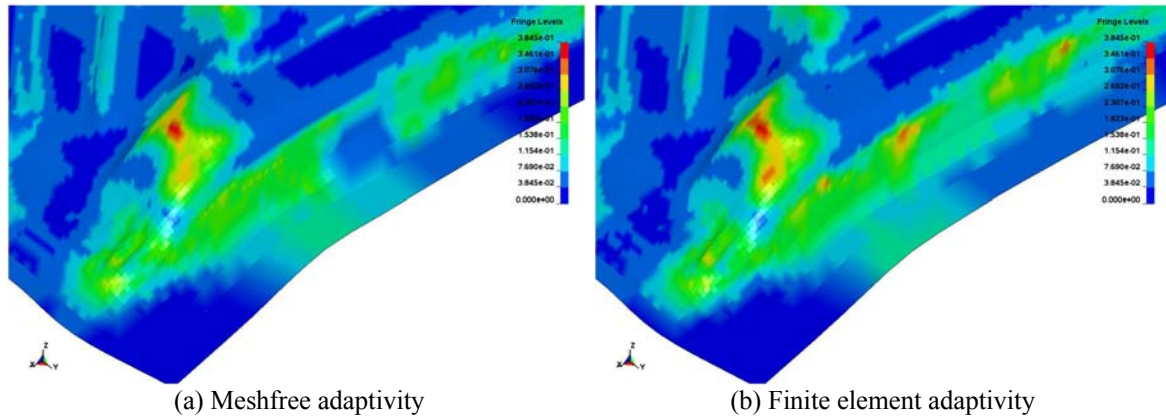
Fig. 12 Comparison of zoom-in effective plastic strain in final shape

element adaptivity 0.55. For the most part of the panel, both methods can capture the deformed geometry with good accuracy and the effective plastic strain contours from the two methods agree well with each other. However, in some areas with tight angle, the effective plastic strain from the finite element adaptivity shows non-smoothness distribution as presented in Fig. 12. This is unrealistic and demonstrates that the finite element adaptivity has difficulty handling geometry with tight angle change. On the other hand, the present meshfree adaptivity generates better results in the complex geometry because of the smooth approximations and a better fit to curved shell structures.

5. Conclusions

This paper presents a meshfree adaptive procedure for dynamic shell structure analysis. The meshfree shell formulation is based on shear deformable shell theory and employs the degenerated continuum and updated co-rotational approach for the finite deformation and large rotation problems. The present meshfree shell formulation is suitable for thin to medium thick shell structures, which often occur in industrial applications. The present meshfree shell adaptive procedure is an h-adaptivity based on the background cells defined on the original configuration. The shape functions of the enriched nodes within the adaptive cells are constructed with the generalized meshfree (GMF) convex approximation and are normalized to possess the Kronecker-delta property. Only the shape functions inside the adaptive cells need to be re-constructed and the transformation matrix does not need to be re-computed, improving the computational efficiency. The proposed meshfree adaptive procedure also ensures compatibility in approximation and satisfaction of integration constraint in spatial integration.

Two numerical examples are employed to demonstrate the performance of the proposed meshfree adaptive procedure. The benchmark reveals that the constraint nodes in the finite element adaptivity prevent it from capturing the necking phenomena in a stretched plate. The sheet metal forming simulation shows that the proposed method has better accuracy than the finite element adaptivity in solving problems with critical geometric feature such as tight angle. The conforming and smooth approximations in the meshfree adaptivity produce smoother stress/strain distribution and fit better to the complex geometry in the shell structures.

Reference

Arroyo, M. and Ortiz, M. (2006), "Local maximum-entropy approximation schemes: a seamless bridge between finite elements and meshfree methods", *Int. J. Numer. Meth. Eng.*, **65**(13), 2167-2202.

Atluri, S.N. and Zhu, T. (1998), "A new meshless local Petrov-Galerkin (MLPG) approach in computational mechanics", *Comput. Mech.*, **22**(2), 117-127.

Babuska, I. and Rheinboldt, W.C. (1978), "A posteriori error estimates for the finite element method", *Int. J. Numer. Meth. Eng.*, **12**(10), 1597-1615.

Baumann, M. and Schweizerhof, K. (1997), "Adaptive mesh generation of arbitrarily curved shell structures", *Comput. Struct.*, **64**(1-4), 209-220.

Belytschko, T., Liu, W.K. and Moran, B. (2000), *Nonlinear finite elements for continua and structures*, John Wiley & Sons, LTD, Chichester, West Sussex, England.

Belytschko, T., Lu, Y.Y. and Gu, L. (1994), "Element-free galerkin methods", *Int. J. Numer. Meth. Eng.*, **37**(2), 229-256.

Belytschko, T. and Tabbara, M. (1993), "H-adaptive finite element methods for dynamic problems, with emphasis on localization", *Int. J. Numer. Meth. Eng.*, **36**(24), 4245-4265.

Blacker, T.D. and Stephenson, M.B. (1991), "Paving: a new approach to automated quadrilateral mesh generation", *Int. J. Numer. Meth. Eng.*, **32**(4), 811-847.

Chen, J.S., Pan, C., Wu, C.T. and Liu, W.K. (1996), "Reproducing kernel particle methods for large deformation analysis of non-linear structures", *Comput. Methods Appl. Mech. Eng.*, **139**(1-4), 195-227.

Chen, J.S., Wu, C.T., Yoon, S. and You, Y. (2001), "A stabilized conforming nodal integration for galerkin mesh-free methods", *Int. J. Numer. Meth. Eng.*, **50**(5), 435-466.

Chen, J.S. and Wang, D. (2006), "A constrained reproducing kernel particle formulation for shear deformable shell in Cartesian coordinates", *Int. J. Numer. Meth. Eng.*, **68**(2), 151-172.

Chung, H.J. and Belytschko, T. (1998), "An error estimate in the EFG method", *Comput. Mech.*, **21**(2), 91-100.

Deb, A., Prevost, J.H. and Loret, B. (1996), "Adaptive meshing for dynamic strain localization", *Comput. Methods Appl. Mech. Eng.*, **137**(3), 285-306.

Hallquist, J.O. (2003), *LS-DYNA Theory manual.*

Hill, R. (1948), "A theory of the yielding and plastic flow of anisotropic metals", *Proceedings of the Royal Society of London, Series A*, **193**, 281.

Lancaster, P. and Salkauskas, K. (1981), "Surfaces generated by moving least squares methods", *Math. Comput.*, **37**(155), 141-158.

Liu, G.R. and Tu, Z.H. (2002), "An adaptive procedure based on background cells for meshless methods", *Comput. Methods Appl. Mech. Eng.*, **191**(17-18), 1923-1943.

Liu, G.R. and Zhang, G.Y. (2008), "Upper bound solution to elasticity problems: A unique property of the linearly conforming point interpolation method (LC-PIM)", *Int. J. Numer. Meth. Eng.*, **74**(7), 1128-1161.

Liu, W.K., Jun, S., Li, S., Adee, J. and Belytschko, T. (1995a), "Reproducing kernel particle methods for structural dynamics", *Int. J. Numer. Meth. Eng.*, **38**(10), 1655-1679.

Liu, W.K., Jun, S. and Zhang, Y.F. (1995b), "Reproducing kernel particle methods", *Int. J. Numer. Meth. Fluids*, **20**(8-9), 1081-1106.

Mar, A. and Hicks, M.A. (1996), "A benchmark computational study of finite element error estimation", *Int. J. Numer. Meth. Eng.*, **39**(23), 3969-3983.

Moes, N., Dolbow, J. and Belytschko, T. (1999), "A finite element method for crack growth without

remeshing", *Int. J. Numer. Meth. Eng.*, **46**(1), 131-150.

Ortiz, M. and Quigley, J.J. (1991), "Adaptive mesh refinement in strain-localization problems", *Comput. Meth. Appl. Mech. Eng.*, **90**(1-3), 781-809.

Pannachet, T., Sluys, L.J. and Askes, H. (2008), "Error estimation and adaptivity for discontinuous failure", *Int. J. Numer. Meth. Eng.*, **78**(5), 528-563.

Park, C.K., Wu, C.T. and Kan, C.D. (2011), "On the analysis of dispersion property and stable time step in meshfree method using the generalized meshfree approximation", *Finite Elem. Anal. Des.*, **47**(7), 683-697.

Rabczuk, T. and Belystchko, T. (2005), "Adaptivity for structured meshfree particle methods in 2D and 3D", *Int. J. Numer. Meth. Eng.*, **63**(11), 1559-1582.

Riccius, J., Schweizerhof, K. and Baumann, M. (1997), "Combination of adaptivity and mesh smoothing for the finite element analysis of shell intersections", *Int. J. Numer. Meth. Eng.*, **40**(13), 2459-2474.

Sheffer, A. and de Sturler, E. (2001), "Parameterization of faceted surfaces for meshing using angle-based flattening", *Eng. Comput.*, **17**(3), 326-337.

Shepard, D. (1968), "A two-dimensional interpolation function for irregularly-spaced data", *Proceedings of the 1968 ACM National Conference*, New York, 517-524, DOI: 10.1145/800186.810616.

Sukumar, N. (2004), "Construction of polygonal interpolants: a maximum entropy approach", *Int. J. Numer. Meth. Eng.*, **61**(12), 2159-2181.

Wang, D. and Chen, J.S. (2004), "Locking-free stabilized conforming nodal integration for meshfree Mindlin-Reissner plate formulation", *Comput. Meth. Appl. Mech. Eng.*, **193**(12-14), 1065-1083.

Wang, D. and Lin, Z. (2011), "Dispersion and transient analyses of hermite reproducing kernel galerkin meshfree method with sub-domain stabilized conforming integration for thin beam and plate structures", *Comput. Mech.*, **48**(1), 47-63.

Wang, D. and Wu, Y. (2008), "An efficient galerkin meshfree analysis of shear deformable cylindrical panels", *Interact. Multiscale Mech.*, **1**(3), 339-355.

Wang, H.P., Wu, C.T., Guo, Y. and Botkin, M.E. (2009), "A coupled meshfree/finite element method for automotive crashworthiness simulations", *Int. J. Impact Eng.*, **36**(10-11), 1210-1222.

Wu, C.T. and Guo, Y. (2002), *Development of coupled finite element/mesh-free method and mesh-free shell formulation*, Technical Report, GM R&D Center.

Wu, C.T. and Guo, Y. (2004), *Development of an adaptive mesh-free shell algorithm and a parallelized coupled finite element/mesh-free shell method incorporating thickness stress for explicit dynamic analysis*, Technical Report, GM R&D Center.

Wu, C.T. and Koishi, M. (2009), "A meshfree procedure for the microscopic analysis of particle-reinforced rubber compounds", *Interact. Multiscale Mech.*, **2**(2), 147-169.

Wu, C.T., Park, C.K. and Chen, J.S. (2011), "A generalized approximation for the meshfree analysis of solids", *Int. J. Numer. Meth. Eng.*, **85**(6), 693-722.

Wu, C.T. and Hu, W. (2011), "Meshfree-enriched simplex elements with strain smoothing for the finite element analysis of compressible and nearly incompressible solids", *Comput. Methods Appl. Mech. Eng.*, **200**(45-46), 2991-3010.

Wu, C.T., Hu, W. and Chen, J.S. (2012), "Meshfree-enriched finite element methods for the compressible and near-incompressible elasticity", *Int. J. Numer. Meth. Eng.*, **90**(7), 882-914.

Zienkiewicz, O.C. and Zhu, J.Z. (1987), "A simple error estimator and adaptive procedure for practical engineering analysis", *Int. J. Numer. Meth. Eng.*, **24**(2), 337-357.